# Search for diboson resonances in hadronic final states in 79.8 fb$^{-1}$ of $pp$ collisions at $\sqrt{s}$ = 13 TeV with the ATLAS detector

The ATLAS Collaboration

Narrow resonances decaying into $WW$, $WZ$ or $ZZ$ boson pairs are searched for in 79.8 fb$^{-1}$ of proton–proton data at a centre-of-mass energy of $\sqrt{s}$ = 13 TeV recorded with the ATLAS detector at the Large Hadron Collider from 2015 to 2017. The diboson system is reconstructed using pairs of high transverse momentum, large-radius jets built from a combination of calorimeter- and tracker-inputs tagged as compatible with the hadronic decay of a boosted $W$ or $Z$ boson, using jet mass and substructure properties. The search covers diboson resonances with masses in the range 1.2 TeV − 5.0 TeV. No significant deviations from the background expectations are seen. Exclusion limits at the 95% confidence level are set on the production cross section times branching ratio to dibosons for a range of theories beyond the Standard Model, with the highest lower limit on the mass of a new gauge boson at 4.15 TeV in the context of mass-degenerate resonances that couple predominantly to bosons.

# 1 Introduction

Searching for new phenomena that may become visible in high-energy proton–proton ($pp$) collisions is one of the main goals of the Large Hadron Collider (LHC). New heavy, multi-TeV scale, resonances of vector bosons $VV$ (where $V$ represents $W$ or $Z$ bosons) are a possible signature of such new physics and are predicted in several extensions to the Standard Model. These include extended gauge symmetry models [1–3], Grand Unified theories [4–7], theories with warped extra dimensions [8–12], two Higgs doublet models [13], little Higgs models [14], theories with new strong dynamics [15], including technicolour [16–18] and more generic composite Higgs models [19]. The large data set of 36 fb$^{-1}$ of $pp$ collisions collected in 2015 and 2016 at the LHC at $\sqrt{s}$ = 13 TeV offered an improvement in sensitivity to heavy diboson resonances. Both the ATLAS and CMS collaboration have performed searches in the fully hadronic final states using this data set. In both results [20, 21], no significant deviation from a smooth background consistent with the Standard Model expectation was observed. Searches from ATLAS [22, 23] and CMS [24, 25] for semileptonic decay modes of the boson pair in Run 2 data did also not reveal any hint of new physics.

This note presents a search for narrow diboson resonances decaying to fully hadronic final states in 79.8 fb$^{-1}$ of $pp$ collision data collected by the ATLAS experiment between 2015 and 2017. $W$ and $Z$ bosons produced in the decay of TeV-scale resonances are highly boosted, and therefore are reconstructed in ATLAS as a single large radius parameter ($R$=1.0) jet. The signature of such heavy resonance decays in this mode is thus a resonant structure in the dijet invariant mass spectrum. Although the hadronic decays of vector bosons have the largest branching ratio (67% for $W$ and 70% for $Z$ bosons), they suffer from a large background contamination from the production of multijet events. Contributions to the background from processes containing real bosons, $V$ + jets, Standard Model $VV$, $t\bar{t}$ and single top production, is significantly smaller. To suppress this orders of magnitude larger background, one can use the characteristic jet substructure of $W/Z$-bosons to reject multijet events.

The sensitivity of this search compared to previous results does not drastically improve by just increasing the size of the data set. One must also improve the underlying techniques used to extract signatures of new physics. Novel developments in the reconstruction of inputs used for jet finding, which improve the jet substructure resolution of ATLAS in highly boosted topologies are such techniques [26]. To further benefit from these developments, a new approach to optimizing the identification of boosted boson candidates is introduced in this note. Together with the larger data set, these novel developments are expected to significantly improve the sensitivity to new resonances compared to previous results. The identification of the boosted boson candidates is validated in a data sample enriched in events from Standard Model $V$ + jets production.

To avoid limitations from poor modelling or limited statistic backgrounds in Monte Carlo (MC) samples, the observed background is characterised by a parametric function fit to the smoothly falling distribution. To assess the sensitivity of the search, to optimise the event selection and for comparison with the observed data, two specific benchmark models are used: a spin-1 Heavy Vector Triplet Model (HVT) [27] which provides signals such as $W' \rightarrow WZ$ and $Z' \rightarrow WW$ and a spin-2 graviton $G_{\mathrm{KK}} \rightarrow WW$ or $ZZ$, corresponding to Kaluza-Klein (KK) modes [8, 9] of the Randall-Sundrum (RS) graviton [10–12].

## 2 Signal Models

Monte Carlo simulation of signal events are used to optimise the sensitivity of the search and to interpret its results. Signals are simulated within two benchmark scenarios.

The first scenario is based on two benchmark models of the HVT phenomenological Lagrangian [27]. The Lagrangian introduces a new heavy vector triplet ($W'$, $Z'$) produced via quark-antiquark annihilation, whose members are degenerate in mass, and parametrizes its couplings with Standard Model fields in a generic manner, such that a large class of extensions to the Standard Model can be described.

Model A with $g_V = 1$ [27] describes scenarios where the new triplet field couples weakly to the Standard Model fields and arises from an extension of the Standard Model gauge group, with the heavy vectors having comparable branching ratios into fermions and gauge bosons. For $W'$ and $Z'$ masses of interest in this note, the width of the new heavy bosons is approximately 2.5%, which results in observable mass peaks with a width dominated by the experimental resolution (see Section 7.3). The branching fraction of the new heavy boson $W'$ ($Z'$) to each of the final states $WZ$, and $WH$ ($WW$ and $ZH$), where $H$ represents the Higgs boson, is approximately 2%. The calculated production cross section times branching ratio ($\sigma \times \mathcal{B}$) values for $W' \rightarrow WZ$ with $W$ and $Z$ bosons decaying hadronically are 8.3 fb and 0.75 fb for $W'$ masses of 2 TeV and 3 TeV, respectively. Corresponding values for $Z' \rightarrow WW$ are 3.8 fb and 0.34 fb.

Model B with $g_V = 3$ is representative of composite Higgs models, where the fermionic couplings are suppressed. For the $W'$ and $Z'$ masses of interest, the branching fraction of the new heavy boson $W'$ ($Z'$) to each of the final states $WZ$, and $WH$ ($WW$ and $ZH$), is close to 50%. Resonance widths and experimental signatures are similar to those obtained for model A and the predicted $\sigma \times \mathcal{B}$ values for $W' \rightarrow WZ$ with hadronic $W$ and $Z$ decays are 13 fb and 1.3 fb for $W'$ masses of 2 TeV and 3 TeV, respectively. Corresponding values for $Z' \rightarrow WW$ are 6.0 fb and 0.55 fb.

The second scenario considered is the so-called bulk RS model [10] which extends the original RS model [8, 28] with a warped extra dimension, by allowing the Standard Model fields to propagate in the bulk of the extra dimension. This model is characterized by a dimensionless coupling constant $\kappa/\bar{M}_{\mathrm{Pl}} \sim 1$, where $\kappa$ is the curvature of the warped extra dimension, and $\bar{M}_{\mathrm{Pl}}$ is the reduced Plank mass. In this model, a Kaluza–Klein graviton, $G_{\mathrm{KK}}$, decays to pairs of top quarks, pairs of Higgs bosons, $WW$ and $ZZ$ with considerable branching fractions. The branching fraction of the $G_{\mathrm{KK}}$ to $WW$ ($ZZ$) ranges from 24% to 20% (12% to 10%) as the mass increases. The decay width of the $G_{\mathrm{KK}}$ is approximately 6% of its pole mass, resulting in observable mass peaks with a width comparable to the experimental resolution (see Section 7.3), and $\sigma \times \mathcal{B}$ for $G_{\mathrm{KK}} \rightarrow WW$ with $W$ decaying hadronically are 0.54 fb and 0.026 fb for $G_{\mathrm{KK}}$ masses of 2 TeV and 3 TeV, respectively. Corresponding values for $G_{\mathrm{KK}} \rightarrow ZZ$ are 0.32 fb and 0.015 fb.

## 3 ATLAS Detector

The ATLAS detector [29] surrounds nearly the entire solid angle around the ATLAS collision point. It has an approximately cylindrical geometry and consists of an inner tracking detector surrounded by electromagnetic and hadronic calorimeters and a muon spectrometer. The tracking detector is placed within a 2 T axial magnetic field provided by a superconducting solenoid and measures charged-particle

trajectories with pixel and silicon microstrip detectors that cover the pseudorapidity[1] range $|\eta| < 2.5$, and with a straw-tube transition radiation tracker covering $|\eta| < 2.0$. A new innermost pixel layer [30] inserted at a radius of 3.3 cm has been used since 2015.

Electromagnetic and hadronic calorimeter systems provide energy measurements with high granularity. The electromagnetic calorimeter is a liquid-argon (LAr) sampling calorimeter with lead absorbers, spanning $|\eta| < 3.2$ with barrel and end-cap sections. The three-layer central hadronic calorimeter comprises scintillator tiles with steel absorbers and extends to $|\eta| = 1.7$. The hadronic end-cap calorimeters measure particles in the region $1.5 < |\eta| < 3.2$ using liquid argon with copper absorbers. The forward calorimeters cover $3.1 < |\eta| < 4.9$, using LAr/copper modules for electromagnetic energy measurements and LAr/tungsten modules to measure hadronic energy.

The muon spectrometer surrounds the calorimetry system. It includes three large superconducting air-core toroids providing a magnetic field for accurate momentum measurements in tracking drift chambers arranged in a barrel, covering $|\eta| < 1.0$, and end-caps, extending to $|\eta| = 2.7$, configuration. Fast trigger chambers are spread throughout the system to allow triggering on muon objects at level-1.

Events are recorded in ATLAS if they satisfy a two-level trigger requirement [31]. The level-1 trigger detects jet and particle signatures in the calorimeter and muon systems with a fixed latency of 2.5 $\mu$s, and is designed to reduce the event rate to about 100 kHz. Jets are identified at level-1 with a sliding-window algorithm, searching for local maxima in square regions with size $\Delta\eta \times \Delta\phi = 0.8 \times 0.8$. The subsequent high-level trigger consists of software-based trigger filters which reduces the event rate to one kHz.

# 4 Data

This search is performed using data collected in 2015, 2016, and 2017 from $\sqrt{s} = 13$ TeV LHC $pp$ collisions. Events used in this search satisfy a single-jet trigger requirement, based on at least one jet reconstructed at each trigger level. The final filter in the high-level trigger requires a jet to satisfy a high transverse momentum ($E_T$) threshold, $E_T \geq 360$ GeV (2015), $E_T \geq 420$ GeV (2016), $E_T \geq 440$ GeV (2017), reconstructed with the anti-$k_t$ algorithm [32] and a large radius parameter ($R$=1.0) and using as inputs calorimeter-cell clusters calibrated to the hadronic scale using the local cell signal weighting (LCW) method [33]. After requiring that the data were collected during stable beam conditions and the detector components relevant to this analysis were functional, the integrated luminosity is 3.2 fb$^{-1}$ in 2015, 33.0 fb$^{-1}$ in 2016, and 43.6 fb$^{-1}$ in 2017.

# 5 Simulation

The search presented here uses simulated MC event samples to optimise the selection criteria, to estimate the acceptance for different signal processes, and to validate the experimental procedure described below. For all MC samples, all hadronic final states are imposed at the generator level.

---

[1] ATLAS uses a right-handed coordinate system with its origin at the nominal interaction point (IP) in the centre of the detector and the $z$-axis along the beam pipe. The $x$-axis points from the IP to the centre of the LHC ring, and the $y$-axis points upward. Cylindrical coordinates $(r, \phi)$ are used in the transverse plane, $\phi$ being the azimuthal angle around the beam pipe. The pseudorapidity is defined in terms of the polar angle $\theta$ as $\eta = -\ln\tan(\theta/2)$. Angular distance is measured in units of $\Delta R = \sqrt{(\Delta\eta)^2 + (\Delta\phi)^2}$.

MC samples for the HVT and RS models, were generated using MADGRAPH 2.2.2 [34] interfaced to PYTHIA v8.186 [35] for hadronization using the NNPDF 2.3 LO parton distribution function (PDF) set [36] and the A14 set of tuned parameters for the underlying event [37]. In all signal samples, the $W$ and $Z$ bosons are primarily longitudinally polarised.

PYTHIA v8.186 with the NNPDF 2.3 LO PDF set and the A14 tune is used to generate and shower multijet background events. Samples of $W$+jets and $Z$+jets events were generated with SHERPA 2.1.1 [38–41] interfaced with the CT10 PDF set [42]. A $t\bar{t}$ sample generated with POWHEG-BOX v2 [43] with the NNPDF 3.0 NLO PDF [44], interfaced with PYTHIA 8 with NNPDF 2.3 LO PDF and A14 ATLAS tune for parton shower is used for the $V$+jets study. EvtGen v1.2.0 [45] is used for properties of bottom and charm hadron decays.

For all MC samples, the final-state particles produced by the generators are propagated through a detailed detector simulation based on GEANT 4 [46, 47]. The mean number of $pp$ interactions per bunch crossing, "pile-up", was approximately 32 while the collision data were collected. The expected contribution from these additional minimum-bias $pp$ interactions is accounted for by overlaying additional minimum-bias events generated with PYTHIA v8.186. MC is weighted to match the distribution of the average number of interactions per bunch crossing observed in collision data. Simulated events are then reconstructed with the same algorithms run on collision data.

# 6 Reconstruction

The objects central to this analysis are the hadronic jets. Since the decay products of TeV-scale resonances are highly boosted, their decay products become increasingly collimated and they therefore are reconstructed as a single jet. It is important that they can still be differentiated with respect to QCD multi-jet events where a jet is initiated by a single quark or gluon. This relies on both the energy and angular resolution of the detector used to reconstruct the jet. Although the analysis primarily relies on jets, lepton candidates are needed to reject events that could bias the Standard Model $V$+jets studies presented in Section 7.2.

## 6.1 Track-CaloClusters

In previous analyses, ATLAS has mainly focused on the use of calorimeter-based jet substructure, which exploits the exceptional energy resolution of the ATLAS calorimetry [33]. However, as the event becomes even more energetic, jets become so collimated that the calorimeter lacks the angular resolution to resolve the desired structure within the jet. For boson jets in the $p_T$ range relevant for this analysis, only a handful of calorimeter-cell clusters are created, each with limited angular resolution, but excellent energy resolution. On the other hand, the tracking detector has excellent angular resolution and good reconstruction efficiency at very high energy [48], while its energy resolution deteriorates. By combining information from the ATLAS calorimeter and tracking detectors, the precision of jet substructure techniques can be improved for a wide range of energies. This analysis uses a new unified object built from both tracking and calorimeter information, referred to as Track-CaloClusters (TCCs) [26]. This procedure is a type of particle flow, complementary to the energy subtraction algorithm described in the recent ATLAS particle flow publication [49] which improves the energy resolution of low energetic jets. The two algorithms are designed to improve the jet reconstruction performance in very different energy regimes, reflected in their distinct four-vector construction and energy sharing procedures. Energy sharing in the TCC approach is

addressed solely based on a weighting scheme where only the relative track momenta are used to spatially redistribute the energy measured in the calorimeter. In practice, this means that the TCC algorithm uses the spatial coordinates of the tracker and the energy scale of the calorimeter. A more detailed description of TCCs can be found in Ref. [26].

## 6.2  Jet reconstruction

This analysis uses anti-$k_t$, $R = 1.0$ jets reconstructed from a combination of combined and neutral TCCs. Combined TCCs are four-vectors created by combining the angular information of tracks with the energy information of the calorimeters. Neutral TCCs are calorimeter topo-clusters which could not be matched to any track, most likely representing energy deposits from neutral particles. The combination of combined and neutral TCCs captures the large majority of the hard scatter energy and provides the best representation of the total energy flow in the event, as there are both charged and neutral contributions. The combined TCC component is robust against effects from pile-up due to the applied track-to-primary-vertex matching requirement. However, by including the neutral TCCs (unmatched topo-clusters), these jets will have a pile-up dependence similar to that of standard topo-cluster jets. Jets are therefore trimmed [50] to remove contributions from pile-up by removing any $R = 0.2$ subjet with less than 5% of the $p_T$ of the associated $R = 1.0$ jet. The clustering and trimming algorithms use the FastJet package [51]. The combination of pile-up suppression through track-to-primary-vertex matching and trimming makes these jet objects very robust against pile-up [26]. A MC based particle-level energy and mass calibration is applied to the jets used in this analysis, as described in Ref. [52]. It is useful to also create truth jets using the same algorithm and trimming procedure, but with inputs of stable generator-level particles ($c\tau > 10$ mm) excluding muons and neutrinos, and excluding particles from pile-up.

Two variables will be used in this analysis to discriminate hadronic decays of $W$ and $Z$ bosons from background jets. One is the jet mass, the other is $D_2$[2], which is defined as a ratio of two-point to three-point energy correlation functions that are based on the energies of the jet's constituents and their pairwise angular separations [53]. Signal jets are expected to peak at $D_2$ values below one, while jets from multijet background have significantly larger values. Figure 1 shows the striking improvement in $D_2$ resolutions[3] achieved with TCC jets. The mass resolution is superior to the previously used jets starting around a jet $p_T$ of 2000 GeV. Below 1000 GeV, the mass resolution in TCC jets is slightly degraded. For identifying hadronically decaying $V$-bosons, the improvement in $D_2$ resolution far outweighs the slight degradation in mass resolution.

## 6.3  Electrons

Electron identification is based on matching tracks to energy clusters in the electromagnetic calorimeter and calculating a likelihood based on several properties of the electron candidate. Electrons are required to have $p_T > 25$ GeV, be found in the central barrel of the detector, $|\eta| < 2.5$, and to satisfy the "medium" identification criterion [54] and to pass the "loose" track-based isolation [54].

---

[2] The angular exponent $\beta$, defined in Ref. [53], is set to unity.

[3] The resolution is defined as $\text{IQR}^r = [Q_{84}(\mathcal{R}^r) - Q_{16}(\mathcal{R}^r)]/[2 \times Q_{50}(\mathcal{R}^r)]$ and $\text{IQR}^d = 1/2\left[Q_{75}(\mathcal{R}^d) - Q_{25}(\mathcal{R}^d)\right]$ for the mass and $D_2$, respectively, where $Q_x$ is the x% quantile boundary, meaning that $Q_{50}$ is the median. The mass response is defined as $\mathcal{R}^r = m_{\text{reco}}/m_{\text{true}}$, while the residual of $D_2$ is $\mathcal{R}^d = D_{2,\text{reco}} - D_{2,\text{true}}$. Truth jets are used as reference "true".

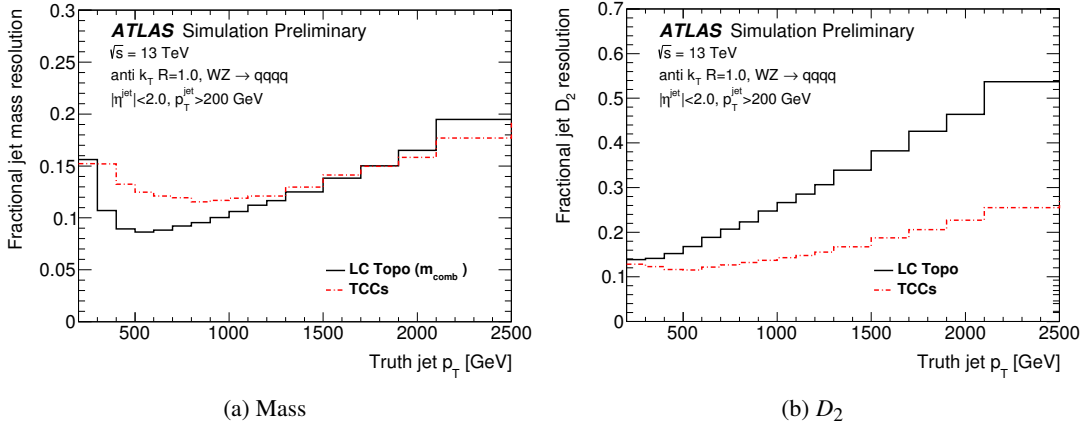|              |              |
| :----------: | :----------: |
| (a) Mass | (b) $D_2$ |

Figure 1: A comparison of the fractional jet (a) mass and (b) $D_2$ resolution for topo-cluster jets (solid black lines), and jets built using combined and neutral TCC objects as a function of truth jet $p_T$. Only the two jets with the highest $p_T$ per event matched to a truth jet from a $W$ or $Z$ boson are shown.

## 6.4 Muons

Muon identification relies on matching tracks in the inner detector to muon spectrometer tracks or track segments. Muons are required to have $p_T > 25$ GeV, be found in the central barrel of the detector, $|\eta| < 2.5$, and to satisfy the "loose" selection criterion [55] and the "loose" track isolation [55].

## 7 Selection

To avoid contamination from non-collision backgrounds such as from calorimeter noise, beam halo, and cosmic rays, events containing an anti-$k_t$ jet built from calorimeter-cell clusters with $R = 0.4$ and $p_T > 20$ GeV failing the loose criteria for consistency with production in $pp$ collisions are rejected [56]. In addition, events with leptons meeting the requirements defined in Section 6 are rejected. There are no further requirements on leptons which are aligned with jets.

Events are required to have at least two anti-$k_t$, $R = 1.0$ jets originating from the primary vertex[4], one with $p_T > 500$ GeV and the second with $p_T > 200$ GeV. The leading (highest $p_T$) and subleading of these jets must be within $|\eta| < 2.0$ (to guarantee a good overlap with the tracking acceptance), have masses $> 50$ GeV, and their invariant mass, $m_{JJ}$, must be larger than 1200 GeV. The last requirement ensures that the used triggers are fully efficient. These selections are referred to as pre-selections.

The pair of jets is then required to have a small separation in rapidity, $|\Delta y_{12}| < 1.2$. This requirement reduces the multi-jet background, which is mainly produced in $t$-channel processes with large rapidity differences, in contrast to signal events which are expected to be produced in $s$-channel processes with small rapidity differences. Additionally, to reject events with potentially badly reconstructed jets, a criterion is applied on the $p_T$ asymmetry, $A = (p_{T1} - p_{T2}) / (p_{T1} + p_{T2}) < 0.15$, where $p_{T1}$ and $p_{T2}$ are the transverse momenta of the leading and subleading jets, respectively.

---

[4] In case more than one vertex is reconstructed, the one with the highest sum of $p_T^2$ of the associated tracks is regarded as the primary vertex.

## 7.1 Boson identification

Jet substructure can be exploited to enhance the separation between signal boson jets and jets from multijet background. Several promising variables have been studied in the past [52], with the largest sensitivity gain coming from the use of the two variables indicated in Section 6.2: jet mass and $D_2$.

A two-dimensional (jet mass, $D_2$) tagger using TCC jets was optimized to provide maximum significance for boosted boson jets with respect to QCD background jets. A measure of significance independent of the cross sections of the new processes searched for was selected: $\epsilon/(a/2 + \sqrt{B})$, where $\epsilon$ is the signal selection efficiency for several masses in the range of 500 GeV to 5000 GeV of the $W'$ model described in Section 2, $a$ is the number of sigma corresponding to a one-sided Gaussian significance, and $B$ is the number of multijet background events after the selection taken from MC simulation [57]. This number does not rely on a specific signal, but is valid for all signals with similar experimental features. Compared to the often used $S/\sqrt{B}$, that breaks down for small values of $B$, as is the case here, this measure is more appropriate. A value of $a = 3$ is used. A two-dimensional optimization is performed, where the value of highest significance in each jet $p_{\mathrm{T}}$ bin is selected as the initial mass window and $D_2$ cut value. The result of this optimization doesn't depend on the event-level selections described at the beginning of this section. Next, the applied cuts on jet mass and $D_2$ are parametrized with a jet $p_{\mathrm{T}}$ dependent function. The resulting smooth cuts for the $W$ and $Z$ boson-tagger as a function of jet $p_{\mathrm{T}}$ are shown in Figure 2. It should be noted that the $W$ and $Z$ boson mass windows overlap.

Contrary to previous boson taggers, the above optimization does not enforce a fixed signal efficiency nor a fixed background rejection, but rather creates a smooth behaviour which maximizes the analysis sensitivity. Figure 3 shows the resulting $W$ and $Z$ boson efficiencies and multijet background rejections (defined as 1/efficiency) as a function of jet $p_{\mathrm{T}}$. The selection cuts retain about 30% efficiency for both $W$- and $Z$-boson jets with $p_{\mathrm{T}} = 500$ GeV. At higher jet $p_{\mathrm{T}}$, the signal efficiency increases, reaching an efficiency close to 60% for jets with a $p_{\mathrm{T}}$ of 2500 GeV. This is motivated by the behaviour of the multijet background, which does decrease rapidly for high dijet masses, and thus higher jet $p_{\mathrm{T}}$. In the regime of $m_{\mathrm{JJ}} > 3.0$ TeV background rejection through boson-tagging is not the main concern of the analysis, which is rather to maintain a reasonable acceptance for signals with small cross-sections. This is also reflected in the background rejection as a function of jet $p_{\mathrm{T}}$. For jets with $p_{\mathrm{T}}$ larger than 2500 GeV the cuts become constant, using the cut value at 2500 GeV.

The radiation of a hard gluon can allow background jets to mimic a two-pronged structure and pass the tagging cuts described above. Discrimination between boson jets and multijet background from such gluon-initiated jets was in previous results attained by cutting on the charged hadron multiplicity, in form of the track multiplicity. The improvement in sensitivity due to such a cut is however relatively low when using TCC jets in combination with the newly designed boson tagger described above. No such selection is therefore applied.

## 7.2 Measurement of boson-tagging efficiency

The modelling of the boson-tagging efficiency is evaluated in a data sample enriched in final states with a vector boson plus jets. This sample is obtained by requiring two jets within $|\eta|<2.0$ and then requesting that the leading jet has a $p_{\mathrm{T}}$ larger than 600 GeV, and that both of the leading jets have a mass over 40 GeV. A higher minimum $p_{\mathrm{T}}$ requirement is imposed on the leading jet than in the nominal event selection to obtain a sample with higher average leading jet $p_{\mathrm{T}}$ that better corresponds to the jet $p_{\mathrm{T}}$ values probed in the

(a) W-tagger: mass window

(b) W-tagger: $D_2$ cut

(c) Z-tagger: mass window
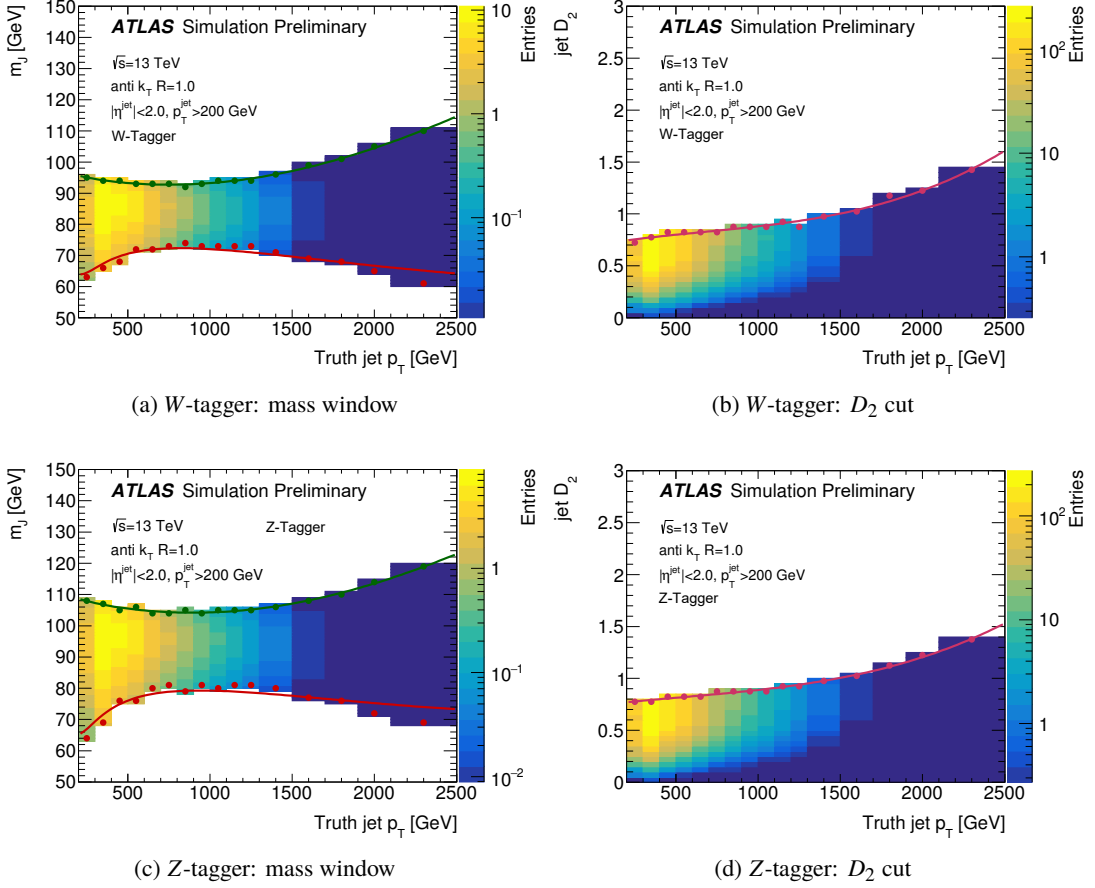
(d) Z-tagger: $D_2$ cut

Figure 2: Jet mass window (a) and $D_2$ cut (b) of the $W$-tagger as a function of jet $p_T$. Corresponding values for the $Z$-tagger are shown in (c) and (d). The initial cut values for maximum significance are shown as solid markers and the fitted parametrizations as solid lines. For illustration, the expected distribution of jets from the used HVT $W' \to WZ$ signal sample is also shown. The tagger is only valid for jets with a $p_T$ between 200 GeV and 2500 GeV and with $|\eta^{jet}| < 2.0$.

search. Events with identified leptons are vetoed. Both jets are independently analysed for the presence of a vector boson, and must pass the $D_2$ selection for either a $W$ or a $Z$ to be considered. The opposite jet is required to fail the same $D_2$ selection to guarantee independence of this control region and the main analysis signal region.

The mass distribution between 50 and 200 GeV of the selected jets is fit by a signal plus background function, allowing to measure the inclusive rate of $W/Z$ plus jets events ($V$ + jets). The contribution originating from $V$ + jets processes is modelled using a double-Gaussian distribution with the shape parameters determined from simulation, while the background contribution is fit to data using a fourth-order exponentiated polynomial. The ability of the fit to extract the correct $V$ + jets yield is tested in simulation and found to be excellent. By comparing the measured event yield in data and MC simulation, potential differences in the selection efficiency ($s_{D_2}$) can be probed. Possible contributions of about 13% from $t\bar{t}$ events are subtracted based on MC simulation. The cross-section of $V$ + jets at a $V$ $p_T$ of about 600 GeV is modelled with about 14% accuracy by the simulation [58]. Additional systematic uncertainties on the fitted $V$ + jets event yield from MC closure, from the uncertainty on the $t\bar{t}$ contribution, as well as
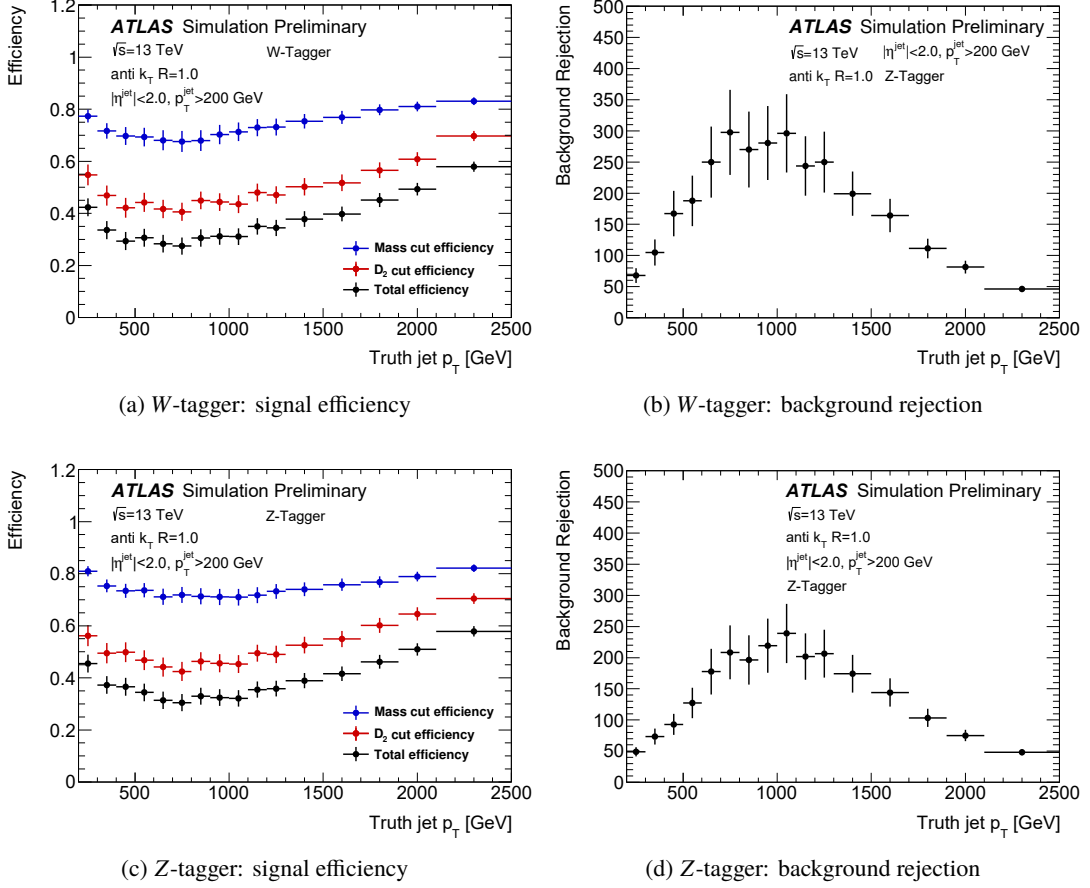
(a) *W*-tagger: signal efficiency

(b) *W*-tagger: background rejection

(c) *Z*-tagger: signal efficiency

(d) *Z*-tagger: background rejection

Figure 3: The (a) signal efficiency and (b) background rejection (1/efficiency) of the *W*-tagger for HVT $W' \rightarrow WZ \rightarrow qqqq$ and QCD multijet MC as a function of the jet $p_T$. Corresponding values for the *Z*-tagger are shown in (c) and (d).

from the fit parametrisation are considered. The relative efficiency of the $D_2$ cut is extracted for *V* bosons with $p_T$ starting from 600 GeV, while the analysis extends to $p_T$ = 2.5 TeV. To estimate the dependence of the modelling on the jet $p_T$, the distribution of the $D_2$ variable is compared in data and MC simulation as a function of jet $p_T$. The observed residual mismodelling as a function of jet $p_T$ is taken into account as an additional 5% uncertainty on the relative efficiency.

The fit to data is shown in Figure 4. Without applying the $D_2$ selection, the contribution from the background would be decreasing with increasing jet mass. This fit only extracts the overall yield, while the width and mean of the $W/Z$ peaks are fixed from similar fits performed on MC simulation. The fitted relative efficiency of the $D_2$ cut in data compared to MC simulation is $s_{D_2} = 0.86 \pm 0.08(\text{stat}) \pm 0.10(\text{closure}) \pm 0.07(t\bar{t}) \pm 0.03(\text{fit}) \pm 0.05(p_T \text{ range}) \pm 0.14(\text{theory})$, or $s_{D_2} = 0.86 \pm 0.21$. Additional fits letting both the width and mean of the $W/Z$ peaks float are used to compare the efficiency of the jet mass window of the boson taggers in data and simulation. Excellent agreement is found, and no additional uncertainty is assigned.
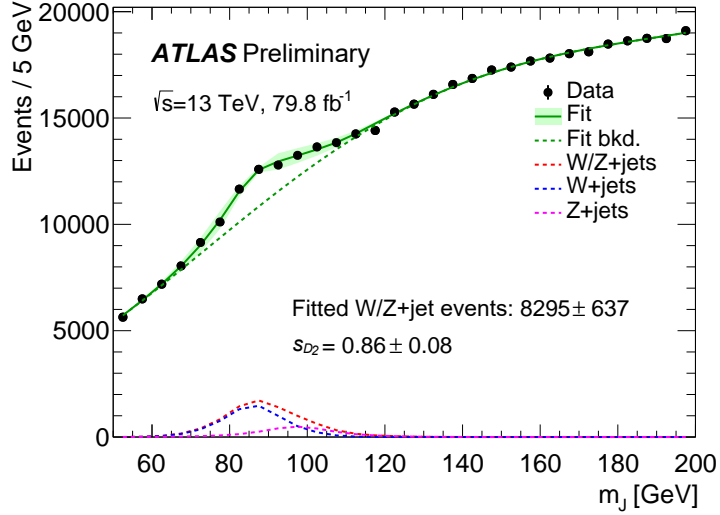
Figure 4: Jet mass distribution for data in the region enhanced in $V$ + jets events after boson tagging based only on the $D_2$ variable. The result of fitting to the sum of functions for the $V$ + jets and background events is also shown. On the bottom, the fitted contribution to the observed jet mass spectra from the $V$ + jets signal is shown. The fitted relative efficiency of the $D_2$ cut is $s_{D_2} = 0.86 \pm 0.08$, where the uncertainty is purely statistical.

## 7.3 Signal and background selection efficiency

After boson-tagging, the data is categorised in five non-exclusive signal regions (SRs): events with two jets identified as $WW$, $ZZ$, and $WZ$, and events with two jets identified as either $WZ$ or $WW$, and either $WW$ or $ZZ$. The selection requirements are summarised in Table 1.

The selection efficiency, defined as the number of selected events at different stages of the selection divided by the number of generated events, as a function of the resonance mass, is shown for the HVT $Z'$ decaying to $WW$ and for the bulk $G_{KK}$ decaying to $ZZ$ in Figure 5. Similar efficiency values are obtained in the $WZ$ final state for the HVT model and in the $WW$ final state for the bulk RS models. Multijet background events are suppressed with a rejection factor of approximately $10^6$ at low $m_{JJ}$ to $10^5$ at $m_{JJ} = 5$ TeV, as determined from simulation. The figure shows that, among the different selection criteria described above, the boson tagging reduces the signal efficiency the most. However, this particular selection stage also provides the most significant suppression of the dominant multijet background. The resulting width of the $m_{JJ}$ distributions in the signal region for a HVT model A $W' \rightarrow WZ$ (Bulk RS graviton $\rightarrow ZZ$) is about 6% (10%) of its mean value across the studied mass range, corresponding to about 120 GeV (200 GeV) at 2 TeV.

## 8 Background Parameterisation

The search for diboson resonances is performed by looking for narrow peaks above the smoothly falling $m_{JJ}$ distribution expected in the Standard Model. The background to the search is estimated empirically from the observed $m_{JJ}$ spectrum in the signal region. The background estimation procedure is based on

11

Table 1: Event selection requirements and definition of the different regions used in the analysis. Different requirements are indicated for the highest-$p_T$ (leading) jet with index 1 and the second highest-$p_T$ (subleading) jet with index 2.

| Signal region | Veto events with leptons: |
|---|---|
| | No $e$ or $\mu$ with $p_T > 25$ GeV and $|\eta| < 2.5$ |
| | Event preselection: |
| | $\geq 2$ large-$R$ jets with $|\eta| < 2.0$ and mass $> 50$ GeV |
| | $p_{T1} > 500$ GeV and $p_{T2} > 200$ GeV |
| | $m_{JJ} > 1.2$ TeV |
| | Topology and boson tag: |
| | $|\Delta y| = |y_1 - y_2| < 1.2$ |
| | $A = (p_{T1} - p_{T2}) / (p_{T1} + p_{T2}) < 0.15$ |
| | Boson tag with $D_2$ variable and $W$ or $Z$ mass window |
| $V$+jets control region | Veto events with leptons |
| | $V$+jets selection: |
| | $\geq 2$ large-$R$ jets with $|\eta| < 2.0$ and mass $> 40$ GeV |
| | $p_{T1} > 600$ GeV and $p_{T2} > 200$ GeV |
| | Boson tag with $D_2$ variable on either jet |
| | Anti-boson tag with $D_2$ variable on other jet |



(a) HVT $Z' \to WW$   (b) RS $G_{KK} \to ZZ$
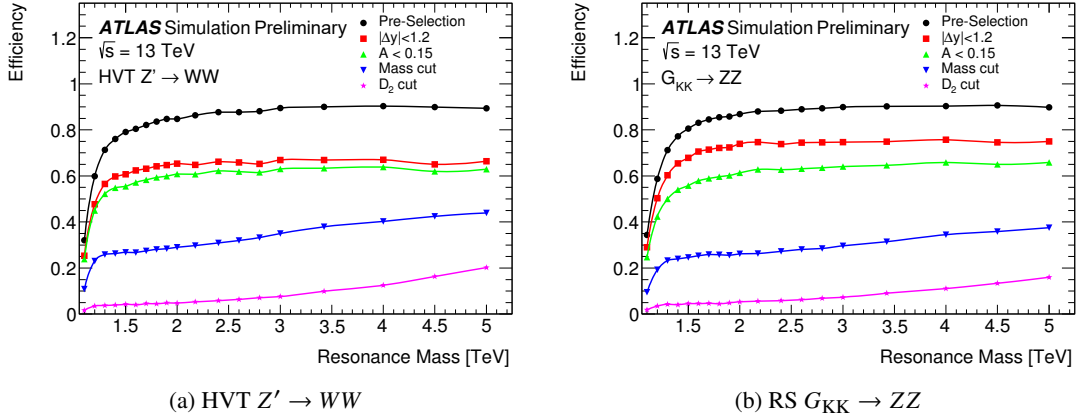
Figure 5: The acceptance × efficiency for the selection, defined as the number of selected events at different stages of the selection divided by the number of generated events, of a HVT $Z' \to WW$ and $G_{KK} \to ZZ$ as a function of mass passing the event selections in sequential. Selections include pre-selections, topological cuts on $|\Delta y_{12}|$, $p_T$ asymmetry, and boson-tagging using jet mass and $D_2$.

a binned maximum-likelihood fit of a parametrized form to the observed $m_{JJ}$ spectrum. The fit uses a parametric form:

$$\frac{dn}{dx} = p_1 (1 - x)^{p_2 - \xi p_3} x^{-p_3} \tag{1}$$

where $x = m_{JJ}/\sqrt{s}$, $p_1$ is a normalization factor, $p_2$ and $p_3$ are dimensionless shape parameters, and $\xi$ is a constant. $\xi$ is derived in an iterative way, minimizing the correlation between $p_2$ and $p_3$ in the fit, for each $m_{JJ}$ distribution. It was confirmed that the complexity of this fit function is sufficient for the expected statistics in the signal regions by performing Wilks likelihood-ratio tests [59]. The fit is performed to the $m_{JJ}$ distribution in each signal region in data with a constant bin size of 100 GeV. This choice is motivated by the experimental resolution.

The modelling of the parametric shape in Eq. 1 is tested in a dedicated fit control region (CR) in data. This CR is designed to resemble the expected background in the SR in both shape and statistics, under the assumption that no signal contribution is present. Using an ABCD-like method, four regions are defined as described in Figure 6. A possible contamination in region A, C, or D from a potential BSM signal is negligible.
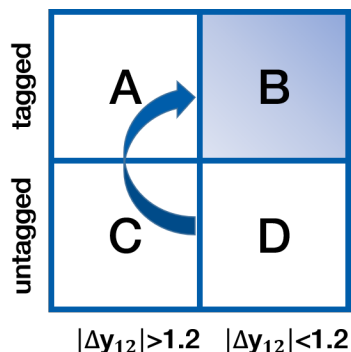


Figure 6: Four orthogonal regions used to build the fit control region. A: $|\Delta y_{12}| > 1.2$ and both jets boson-tagged, B: $|\Delta y_{12}| < 1.2$ and both jets boson-tagged (this is the nominal signal region), C: $|\Delta y_{12}| > 1.2$ and event not boson-tagged, D: $|\Delta y_{12}| < 1.2$ and event not boson-tagged. Regions A and C are used to derive a per-event transfer factor to go from region D to the fit control region, which is representative of region B. A and C are also signal depleted due to the $|\Delta y_{12}| > 1.2$ requirement.

The probability to misidentify a single-jet as a $W$ or $Z$ boson in a data set dominated by QCD multi-jets is parametrized as a function of jet $p_T$ using regions C and A. It has been validated on data that such a probability is independent of $|\Delta y_{12}|$. Since a correlation between the two leading jets of the QCD background is observed after the pre-selections, the probability of the subleading-mass jet is derived requiring the leading-mass jet to pass the boson-taggers' mass window. By applying per jet weights depending on the jet $p_T$ to events in region D, it is transformed to what looks like region B - the fit CR. To correctly take into account the expected statistical fluctuations and uncertainties, the CR distribution is assigned the correct Poisson errors, and fluctuated accordingly. The last step is repeated multiple times, fitting each distribution with the background fit function, and evaluating the goodness-of-fit $\chi^2/\text{NDF}$. Bins with fewer than five events are grouped with bins that contain at least five events to compute the number of degrees of freedom. On average, the $\chi^2/\text{NDF}$ is equal to unity with no stark outliers. Figure 7 shows the fit result performed in an example $WZ$ fit CR of the full 2015-2017 data set. Similar results are obtained for the other CRs confirming the ability of the chosen background fit function (Equation 1) to describe the expected dijet mass spectra in the SRs.

The statistical uncertainty on the background expectation comes directly from the uncertainty on the fitted parameters of the background function, which assumes a smoothly falling $m_{JJ}$ distribution. Possible additional uncertainties due to the background model are assessed by considering signal plus background
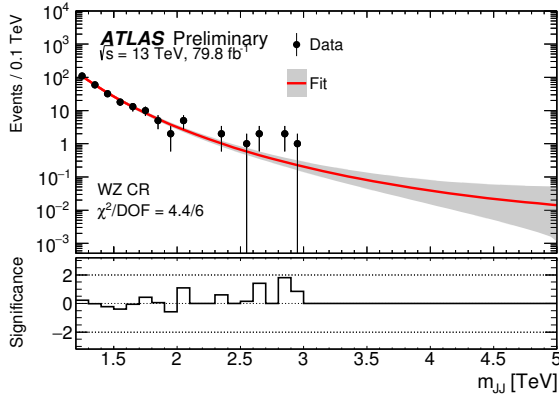
Figure 7: Comparison between fitted background shape and the $m_{\mathrm{JJ}}$ spectra in an example $WZ$ fit control region in data. The fitted background distribution is normalized to the data shown in the displayed mass range. The shaded bands represent the uncertainty on the background expectation calculated from the maximum likelihood function. The lower panels show the significance, defined as the $z$-value as described in Ref. [60].

fits (also called signal spurious tests) of the chosen function to the fit control regions of data in which a signal contribution is expected to be negligible. The background is modelled with Eq. (1) and the signal is modelled using resonance mass distributions from simulation. These effects were estimated to introduce a bias smaller than 25% of the statistical uncertainty on the background estimate at any mass in the search region, and no additional uncertainty is assigned.

# 9 Systematic Uncertainties

The uncertainties affecting the background modelling are taken directly from the errors on the fit parameters of background estimation procedure described in Section 8. The systematic uncertainties on the expected signal yield and shapes arise from detector effects and MC modelling and are assessed and expressed in terms of nuisance parameters in the statistical analysis as shown in Section 10. The dominant sources of uncertainty in the signal modelling arise from uncertainties in the large-$R$ jet tagging efficiency and the jet $p_{\mathrm{T}}$ calibration.

Uncertainty in the jet $p_{\mathrm{T}}$ scale ($Jp_{\mathrm{T}}S$) is evaluated using track-to-calorimeter double ratios between data and MC [61]. The ratio of the calorimeter and track measures of jet $p_{\mathrm{T}}$ is expected to be the same in data and MC and any observed differences are assigned as baseline systematic uncertainties. Uncertainties obtained from this procedure assume no correlation between the two $p_{\mathrm{T}}$ measures, while any residual correlation would increase them by a certain factor. Since the $Jp_{\mathrm{T}}S$ uncertainty has little impact on the sensitivity of the analysis, this correlation is not studied in detail, but rather a conservative factor of two is chosen to cover the strongest possible correlation. Additional uncertainties due to the track reconstruction efficiency, track impact parameter resolution, track fake rate are taken into account. The size of the total $Jp_{\mathrm{T}}S$ uncertainty varies with jet $p_{\mathrm{T}}$ and is between 5% and 10% for the full mass range.

The impact of the jet $p_{\mathrm{T}}$ resolution uncertainty is evaluated event-by-event by rerunning the analysis applying an additional Gaussian smearing of the input jets $p_{\mathrm{T}}$, degrading the nominal resolution by the

14

systematic uncertainty value. The systematic uncertainty in the width of the Gaussian is an absolute 2% per jet, and is symmetrized.

Uncertainty in the jet mass scale and resolution influence the observed jet mass, affecting the boson-tagging efficiency. Any uncertainty on the value of the boson tagging discriminant $D_2$, would also affect the selection efficiency of the analysis. A scale-factor on the $W/Z$-tagging efficiency is derived as described in Section 7.2. The changes to the overall yield is hence corrected by $0.74^{+0.34}_{-0.28}$ per event with the boson-tagging efficiency scale-factor, assuming full correlation between the two jets. The uncertainty on the scale factor is assigned as a two-sided variation on the yield.

The uncertainty in the combined 2015-2017 integrated luminosity is 2.0%. It is derived, following a methodology similar to that detailed in Ref. [62], from a calibration of the luminosity scale using x-y beam-separation scans performed in August 2015 and May 2016 and July 2017 (the results for 2017 are still preliminary). The uncertainty from the trigger selection is found to be negligible, as the minimum requirement on the dijet invariant mass of 1.2 TeV guarantees that the trigger is fully efficient.

Uncertainties in the behaviour of the PDFs at the high $Q^2$ values explored in this analysis can potentially have a large effect on the signal acceptance. This systematic uncertainty is explored by taking the envelope formed by the largest deviations produced by the error sets of three PDF sets, as set out by the PDF4LHC group [63]. A constant 1% uncertainty is applied in the case of the RS model, and a pole mass dependent uncertainty ranging from one to twelve percent is applied in the case of the HVT model. Five pairs of systematic variations are used to cover uncertainties in the A14 tuning parameters describing Initial State Radiation, Final State Radiation, and Multi-Parton Interaction. The uncertainty on the signal acceptance is evaluated at truth level, before boson tagging cuts. Following the same procedure as for the PDFs, constant uncertainties of 3% (5%) are applied for the HVT (RS) models.

# 10 Results

## 10.1 Background fit

Figures 8 compares the dijet mass distributions of the selected events in the combined $WZ + WW$ and $WW + ZZ$ signal regions with the expected background distribution from the background-only fits to the data. The fitted background functions shown, labelled "Fit", are evaluated in bins between 1.2 TeV and 6.0 TeV. No events are observed beyond 5.0 TeV. A total of 355 and 386 events are observed within 1.2 TeV $< m_{JJ} <$ 5.0 TeV in the $WW + WZ$, and $WW + ZZ$ signal regions, respectively. Due to the non-exclusive selections of the boson-taggers, about 50% of events passing the $WW$ selection also pass the $ZZ$ selection.

## 10.2 Statistical analysis

In the statistical analysis, the parameter of interest is the *signal strength*, which is defined as a scale factor to the predicted signal normalisation of the model being tested. The analysis follows the Frequentist approach with a test statistic based on the profile-likelihood ratio [64]. The test statistic extracts information on the
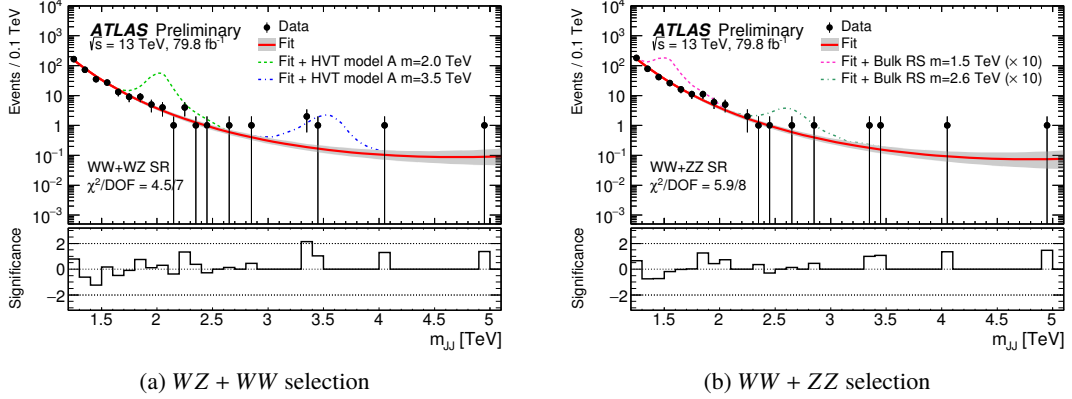
(a) $WZ + WW$ selection            (b) $WW + ZZ$ selection

Figure 8: Background-only fits to the dijet mass ($m_{JJ}$) distributions in data after tagging in the combined (a) $WZ+WW$, and (b) $WW + ZZ$ signal region. The significance shown in the inset for each bin is the difference between the data and the fit in units of the uncertainty on this difference.

signal strength from the binned maximum-likelihood fit of the signal-plus-background model to the data. The likelihood model is defined as,

$$\mathcal{L} = \prod_i P_{\text{pois}}(n^i_{\text{obs}}|n^i_{\text{exp}}) \times G(\alpha) \times \mathcal{N}(\theta) \qquad (2)$$

where $P_{\text{pois}}(n^i_{\text{obs}}|n^i_{\text{exp}})$ is the Poisson probability to observe $n^i_{\text{obs}}$ events if $n^i_{\text{exp}}$ events are expected, $G(\alpha)$ are a series of Gaussian probability density functions modelling the systematic uncertainties, $\alpha$, related to the shape of the signal, and $\mathcal{N}(\theta)$ is a log-normal distribution for the nuisance parameters, $\theta$, modelling the systematic uncertainty on the signal normalisation. The expected number of events is the bin-wise sum of those expected for the signal and background: $\mathbf{n}_{\text{exp}} = \mathbf{n}_{\text{sig}} + \mathbf{n}_{\text{bg}}$. The number of expected background events in dijet mass bin $i$, $n^i_{\text{bg}}$, is obtained by integrating $dn/dx$ obtained from Equation 1 over that bin. Thus $\mathbf{n}_{\text{bg}}$ is a function of the dijet background parameters $p_1, p_2, p_3$. The number of expected signal events, $\mathbf{n}_{\text{sig}}$, is evaluated based on MC simulation assuming the cross section of the model under test multiplied by the signal strength and including the effects of the systematic uncertainties described in Section 9.

The significance of observed excesses over the background-only prediction is quantified using the local $p_0$-value, defined as the probability of the background-only model to produce a signal-like fluctuation at least as large as observed in the data. This value is purely statistical, and no systematic uncertainties are considered. In this analysis, the most extreme $p_0$ has a local significance of 1.8 standard deviations, and is found when testing the HVT $W' \rightarrow WZ$ hypothesis at a resonance mass of 3.5 TeV. This is within the expected fluctuation of the background.

Upper limits at the 95% confidence level (CL) on the production cross section times branching fraction to diboson final states for the benchmark signals are set with the modified-frequentist $CL_s$ prescription [65] using the lowest order asymptotic approximation [64]. All systematic uncertainties are considered. The cross section limits extracted for the different benchmark scenarios in the two signal regions are shown in Fig. 9. A spin-1 vector triplet with couplings predicted by the HVT model A (B) with $g_V = 1$ ($g_V = 3$) is excluded in the range 1.20 TeV < $m(V')$ < 3.40 TeV (1.20 TeV < $m(V')$ < 4.15 TeV), at the 95% confidence level (CL). Production of a $G_{KK}$ in the bulk RS model with $k/\overline{M}_{\text{Pl}} = 1$ is excluded in the ranges

16

Table 2: Observed excluded resonance masses (at 95% CL) in the individual and combined signal regions for the HVT and bulk RS models.

| Model | Signal Region | Excluded mass range [TeV] |
|---|---|---|
| HVT model A, $g_V = 1$ | $WW$ | $1.30 - 2.80$ |
| | $WZ$ | $1.20 - 3.10$ |
| | $WW + WZ$ | $1.20 - 3.40$ |
| HVT model B, $g_V = 3$ | $WW$ | $1.30 - 3.10$ |
| | $WZ$ | $1.20 - 3.30$ |
| | $WW + WZ$ | $1.20 - 4.15$ |
| Bulk RS, $k/\overline{M}_{Pl} = 1$ | $WW$ | $1.30 - 1.60$ |
| | $ZZ$ | *None* |
| | $WW + ZZ$ | $1.20 - 1.90, 2.10 - 2.30$ |

1.20 TeV $< m(G_{KK}) <$ 1.90 TeV and 2.1 TeV $< m(G_{KK}) <$ 2.3 TeV, at the 95% CL. Table 2 presents the resonance mass ranges excluded at the 95% CL in the various signal regions and signal models considered in the search.



(a) HVT $V' \to WW + WZ$

(b) Bulk RS graviton decaying to $WW + ZZ$
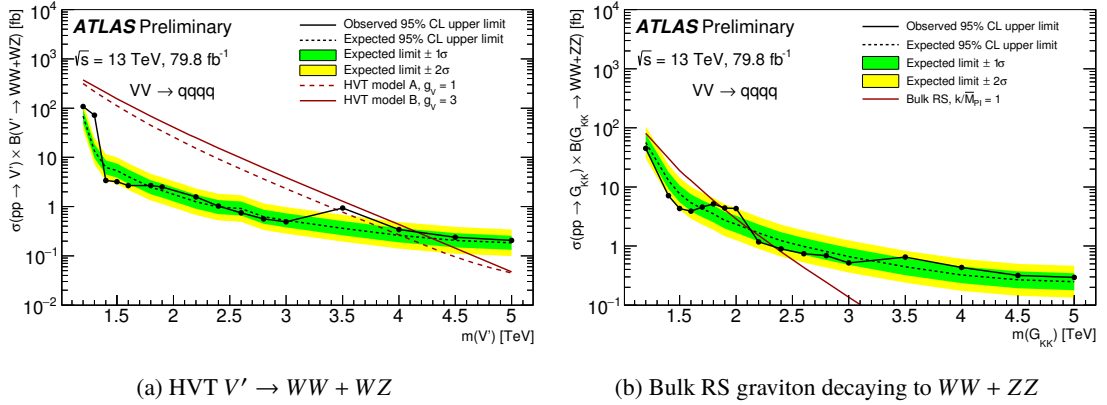
Figure 9: Observed and expected limits at 95% C.L. on cross section times branching ratio for (a) $WW + WZ$ production as a function of $m_{V'}$ and (b) $WW + ZZ$ production as a function of the Bulk RS graviton $m_{G_{KK}}$. The predicted cross section times branching ratio is shown (a) as dashed and solid lines for the HVT models A with $g_V = 1$ and B with $g_V = 3$, respectively, and (b) as a solid line for the bulk RS model with $k/\overline{M}_{Pl} = 1$.

This analysis is able to largely improve on past results mostly due to the use of novel techniques. This can be shown by extrapolating the expected limits from the previous results [20] to the current dataset size, assuming no change to the previous analysis strategy or its uncertainties. The expected limits on cross section times branching fraction would roughly improve by $\times\sqrt{L_{2015-2017}/L_{2015-2016}}$ for the $m_{JJ}$ range which was not statistically limited, and $\times L_{2015-2017}/L_{2015-2016}$ for the high mass range where no events were observed, where $L$ is the integrated luminosity of the respective data sets. The improvement in expected limits for the $WW + WZ$ channel at 3 TeV (5 TeV) is about a factor two (four) larger than expected just from the increased size of the dataset.

# 11 Conclusions

A search for heavy resonances decaying to dibosons in the all hadronic channel has been presented. The search uses 79.8 fb$^{-1}$ of proton-proton collisions at $\sqrt{s}$ = 13 TeV collected by the ATLAS experiment at the LHC from 2015 to 2017. The results of the search are shown for the $WW + WZ$, $WW + ZZ$ channels, and are interpreted in terms of two HVT benchmark models and a bulk $G_{KK}$ model. The data are in agreement with the background expectations in all channels. Upper limits on the production cross section times branching ratio to diboson final states for new resonances with masses between 1.2 and 5.0 TeV are set at the 95% CL. These results exclude at the 95% CL the production of $WW + WZ$ from the HVT model A (model B) with $g_V = 1$ ($g_V = 3$) with masses in the range of 1.20 TeV- 3.40 TeV (1.20 TeV- 4.15 TeV). Production of a $G_{KK}$ in the bulk RS model with $k/\overline{M}_{Pl} = 1$ is excluded in the range 1.20 TeV- 1.90 TeV and 2.1 TeV- 2.3 TeV, at the 95% CL. This analysis is able to improve on past results mostly due to the use of novel reconstruction and analysis techniques. The improvement in expected limits for the $WW + WZ$ channel at 3 TeV (5 TeV) is about a factor two (four) larger than expected just from the increased size of the dataset.

# References

[1] G. Altarelli, B. Mele and M. Ruiz-Altaba,
*Searching for New Heavy Vector Bosons in $p\bar{p}$ Colliders*, Z. Phys. C **45** (1989) 109.

[2] E. Eichten, I. Hinchliffe, K. D. Lane and C. Quigg, *Super Collider Physics*,
Rev. Mod. Phys. **56** (1984) 579.

[3] C. Quigg, *Gauge Theories of the Strong, Weak, and Electromagnetic Interactions*,
Princeton University Press (2013) 227.

[4] J. C. Pati and A. Salam, *Lepton Number as the Fourth Color*, Phys. Rev. D **10** (1974) 275.

[5] H. Georgi and S. Glashow, *Unity of All Elementary Particle Forces*,
Phys. Rev. Lett. **32** (1974) 438.

[6] H. Georgi, *The State of the Art - Gauge Theories. (Talk)*, AIP Conf. Proc. **23** (1975) 575.

[7] H. Fritzsch and P. Minkowski, *Unified Interactions of Leptons and Hadrons*,
Annals Phys. **93** (1975) 193.

[8] L. Randall and R. Sundrum, *A Large mass hierarchy from a small extra dimension*,
Phys. Rev. Lett. **83** (1999) 3370, arXiv: `hep-ph/9905221 [hep-ph]`.

[9] T. Han, J. D. Lykken and R.-J. Zhang, *On Kaluza-Klein states from large extra dimensions*,
Phys. Rev. D **59** (1999) 105006, arXiv: `hep-ph/9811350 [hep-ph]`.

[10] K. Agashe, H. Davoudiasl, G. Perez and A. Soni, *Warped Gravitons at the LHC and Beyond*,
Phys. Rev. D **76** (2007) 036006, arXiv: `hep-ph/0701186 [hep-ph]`.

[11] O. Antipin, D. Atwood and A. Soni, *Search for RS gravitons via $W_L W_L$ decays*,
Phys. Lett. B **666** (2008) 155, arXiv: `0711.3175 [hep-ph]`.

[12] O. Antipin and A. Soni, *Towards establishing the spin of warped gravitons*,
JHEP **0810** (2008) 018, arXiv: `0806.3427 [hep-ph]`.

[13] G. C. Branco et al., *Theory and phenomenology of two-Higgs-doublet models*,
Phys. Rept. **516** (2012) 1, arXiv: `1106.0034 [hep-ph]`.

[14] M. Perelstein, *Little Higgs models and their phenomenology*,
Progress in Particle and Nuclear Physics **58** (2007) 247.

[15] F. Sannino, *Technicolor and Beyond: Unification in Theory Space*,
Journal of Physics: Conference Series **259** (2010) 012003.

[16] E. Eichten and K. Lane, *Low-scale technicolor at the Tevatron and LHC*,
Phys. Lett. B **669** (2008) 235, arXiv: `0706.2339 [hep-ph]`.

[17] S. Catterall, L. Del Debbio, J. Giedt and L. Keegan, *MCRG Minimal Walking Technicolor*,
Phys. Rev. D **85** (2012) 094501, arXiv: `1108.3794 [hep-ph]`.

[18] J. Andersen, O. Antipin, G. Azuelos, L. Del Debbio, E. Del Nobile et al.,
*Discovering Technicolor*, Eur. Phys. J. Plus **126** (2011) 81, arXiv: `1104.1255 [hep-ph]`.

[19] D. Barducci, A. Belyaev, S. Moretti, S. De Curtis and G. M. Pruna,
*LHC physics of extra gauge bosons in the 4D Composite Higgs Model*,
EPJ Web Conf. **60** (2013) 20049.

[20] ATLAS Collaboration, *Search for diboson resonances with boson-tagged jets in pp collisions at* $\sqrt{s}$ = 13 *TeV with the ATLAS detector*, Phys. Lett. B **777** (2018) 91, arXiv: 1708.04445 [hep-ex].

[21] CMS Collaboration, *Search for massive resonances decaying into WW, WZ, ZZ, qW, and qZ with dijet final states at* $\sqrt{s}$ = 13 *TeV*, (2017), arXiv: 1708.05379 [hep-ex].

[22] ATLAS Collaboration, *Search for WW/WZ resonance production in* $\ell\nu qq$ *final states in pp collisions at* $\sqrt{s}$ = 13 *TeV with the ATLAS detector*, JHEP **03** (2018) 042, arXiv: 1710.07235 [hep-ex].

[23] ATLAS Collaboration, *Searches for heavy ZZ and ZW resonances in the* $\ell\ell qq$ *and* $\nu\nu qq$ *final states in pp collisions at* $\sqrt{s}$ = 13 *TeV with the ATLAS detector*, JHEP **03** (2018) 009, arXiv: 1708.09638 [hep-ex].

[24] A. M. Sirunyan et al., *Search for a new heavy resonance decaying into a Z boson and a Z or W boson in 2ℓ2q final states at* $\sqrt{s}$ = 13 *TeV*, (2018), arXiv: 1803.10093 [hep-ex].

[25] A. M. Sirunyan et al., *Search for a heavy resonance decaying into a Z boson and a vector boson in the* $\nu\bar{\nu}q\bar{q}$ *final state*, (2018), arXiv: 1803.03838 [hep-ex].

[26] ATLAS Collaboration, *Improving jet substructure performance in ATLAS using Track-CaloClusters*, ATL-PHYS-PUB-2017-015, 2017, URL: https://cds.cern.ch/record/2275636.

[27] D. Pappadopulo, A. Thamm, R. Torre and A. Wulzer, *Heavy vector triplets: bridging theory and data*, Journal of High Energy Physics **2014**, 60 (2014).

[28] L. Randall and R. Sundrum, *An Alternative to compactification*, Phys. Rev. Lett. **83** (1999) 4690, arXiv: hep-th/9906064 [hep-th].

[29] ATLAS Collaboration, *The ATLAS Experiment at the CERN Large Hadron Collider*, JINST **3** (2008) S08003.

[30] ATLAS Collaboration, *ATLAS Insertable B-Layer Technical Design Report*, (2010), URL: http://cds.cern.ch/record/1291633, ATLAS Insertable B-Layer Technical Design Report Addendum, ATLAS-TDR-19-ADD-1 (2012), URL: http://cds.cern.ch/record/1451888.

[31] ATLAS Collaboration, *Performance of the ATLAS Trigger System in 2015*, Eur. Phys. J. C **77** (2017) 317, arXiv: 1611.09661 [hep-ex].

[32] M. Cacciari, G. P. Salam and G. Soyez, *The anti-$k_T$ jet clustering algorithm*, JHEP **04** (2008) 063.

[33] ATLAS Collaboration, *Topological cell clustering in the ATLAS calorimeters and its performance in LHC Run 1*, Eur. Phys. J. C **77** (2017) 490, arXiv: 1603.02934 [hep-ex].

[34] J. Alwall et al., *The automated computation of tree-level and next-to-leading order differential cross sections, and their matching to parton shower simulations*, JHEP **07** (2014) 079, arXiv: 1405.0301 [hep-ph].

[35] T. Sjöstrand, S. Mrenna and P. Z. Skands, *A Brief Introduction to PYTHIA 8.1*, Comput. Phys. Commun. **178** (2008) 852, arXiv: 0710.3820 [hep-ph].

[36] S. Carrazza, S. Forte and J. Rojo, 'Parton Distributions and Event Generators',
*Proceedings, 43rd International Symposium on Multiparticle Dynamics (ISMD 13)*, 2013 89,
arXiv: 1311.5887 [hep-ph],
URL: http://inspirehep.net/record/1266070/files/arXiv:1311.5887.pdf.

[37] ATLAS Collaboration, *ATLAS Pythia 8 tunes to 7 TeV data*, ATL-PHYS-PUB-2014-021, 2014,
URL: https://cds.cern.ch/record/1966419.

[38] T. Gleisberg, S. Höche, F. Krauss, M. Schönherr, S. Schumann et al.,
*Event generation with SHERPA 1.1*, JHEP **02** (2009) 007, arXiv: 0811.4622 [hep-ph].

[39] S. Höche, F. Krauss, S. Schumann and F. Siegert, *QCD matrix elements and truncated showers*,
JHEP **05** (2009) 053, arXiv: 0903.1219 [hep-ph].

[40] T. Gleisberg and S. Höche, *Comix, a new matrix element generator*, JHEP **12** (2008) 039,
arXiv: 0808.3674 [hep-ph].

[41] S. Schumann and F. Krauss,
*A Parton shower algorithm based on Catani-Seymour dipole factorisation*, JHEP **03** (2008) 038,
arXiv: 0709.1027 [hep-ph].

[42] H.-L. Lai et al., *New parton distributions for collider physics*, Phys. Rev. D **82** (2010) 074024,
arXiv: 1007.2241 [hep-ph].

[43] S. Frixione and B. R. Webber, *Matching NLO QCD computations and parton shower simulations*,
JHEP **06** (2002) 029, arXiv: hep-ph/0204244 [hep-ph].

[44] R. D. Ball et al., *Parton distributions for the LHC Run II*, JHEP **04** (2015) 040,
arXiv: 1410.8849 [hep-ph].

[45] D. J. Lange, *The EvtGen particle decay simulation package*,
Nuclear Instruments and Methods in Physics Research Section A: Accelerators, Spectrometers,
Detectors and Associated Equipment **462** (2001) 152, BEAUTY2000, Proceedings of the 7th Int.
Conf. on B-Physics at Hadron Machines, ISSN: 0168-9002,
URL: http://www.sciencedirect.com/science/article/pii/S0168900201000894.

[46] S. Agostinelli et al., *GEANT4 – a simulation toolkit*, Nucl. Instrum. Meth. A **506** (2003) 250.

[47] ATLAS Collaboration, *The ATLAS Simulation Infrastructure*, Eur. Phys. J. C **70** (2010) 823,
arXiv: 1005.4568 [physics.ins-det].

[48] ATLAS Collaboration,
*Performance of the ATLAS track reconstruction algorithms in dense environments in LHC Run 2*,
Eur. Phys. J. C **77** (2017) 673, arXiv: 1704.07983 [hep-ex].

[49] ATLAS Collaboration,
*Jet reconstruction and performance using particle flow with the ATLAS Detector*,
Eur. Phys. J. C **77** (2017) 466, arXiv: 1703.10485 [hep-ex].

[50] D. Krohn, J. Thaler and L.-T. Wang, *Jet Trimming*, JHEP **02** (2010) 084,
arXiv: 0912.1342 [hep-ph].

[51] M. Cacciari, G. P. Salam and G. Soyez, *FastJet User Manual*, Eur. Phys. J. C **72** (2012) 1896,
arXiv: 1111.6097 [hep-ph].

[52] ATLAS Collaboration, *Identification of Boosted, Hadronically-Decaying W and Z Bosons in
$\sqrt{s} = 13$ TeV Monte Carlo Simulations for ATLAS*, ATL-PHYS-PUB-2015-033, 2015,
URL: https://cds.cern.ch/record/2041461.

[53] A. J. Larkoski, G. P. Salam and J. Thaler, *Energy Correlation Functions for Jet Substructure*, JHEP **1306** (2013) 108, arXiv: `1305.0007 [hep-ph]`.

[54] ATLAS Collaboration, *Electron efficiency measurements with the ATLAS detector using the 2015 LHC proton–proton collision data*, ATLAS-CONF-2016-024, 2016, URL: `https://cds.cern.ch/record/2157687`.

[55] ATLAS Collaboration, *Muon reconstruction performance of the ATLAS detector in proton–proton collision data at $\sqrt{s}$ = 13 TeV*, Eur. Phys. J. C **76** (2016) 292, arXiv: `1603.05598 [hep-ex]`.

[56] ATLAS Collaboration, *Selection of jets produced in 13 TeV proton–proton collisions with the ATLAS detector*, ATLAS-CONF-2015-029, 2015, URL: `https://cds.cern.ch/record/2037702`.

[57] G. Punzi, *Sensitivity of searches for new signals and its optimization*, eConf **C030908** (2003) MODT002, [,79(2003)], arXiv: `physics/0308063 [physics]`.

[58] U. Blumenschein et al., 'Pushing the precision frontier at the LHC with V+jets', 2018, arXiv: `1802.02100 [hep-ex]`, URL: `https://inspirehep.net/record/1653450/files/1802.02100.pdf`.

[59] S. S. Wilks, *The Large-Sample Distribution of the Likelihood Ratio for Testing Composite Hypotheses*, Annals Math. Statist. **9** (1938) 60.

[60] Choudalakis, G. and Casadei, D., *Plotting the differences between data and expectation*, Eur. Phys. J. Plus **127** (2012) 25.

[61] ATLAS Collaboration, *Performance of jet substructure techniques for large-R jets in proton–proton collisions at $\sqrt{s}$ = 7 TeV using the ATLAS detector*, JHEP **09** (2013) 076, arXiv: `1306.4945 [hep-ex]`.

[62] ATLAS Collaboration, *Luminosity determination in pp collisions at $\sqrt{s}$ = 8 TeV using the ATLAS detector at the LHC*, Eur. Phys. J. C **76** (2016) 653, arXiv: `1608.03953 [hep-ex]`.

[63] J. Butterworth et al., *PDF4LHC recommendations for LHC Run II*, J. Phys. G **43** (2016) 023001, arXiv: `1510.03865 [hep-ph]`.

[64] G. Cowan, K. Cranmer, E. Gross and O. Vitells, *Asymptotic formulae for likelihood-based tests of new physics*, Eur.Phys.J.C **71** (2011) 1554, arXiv: `1007.1727 [physics.data-an]`.

[65] A. L. Read, *Modified frequentist analysis of search results (the CLs method)*, CERN-OPEN-2000-205 (2000).

# Appendix

(a) W-tagger: mass window

(b) W-tagger: $D_2$ cut

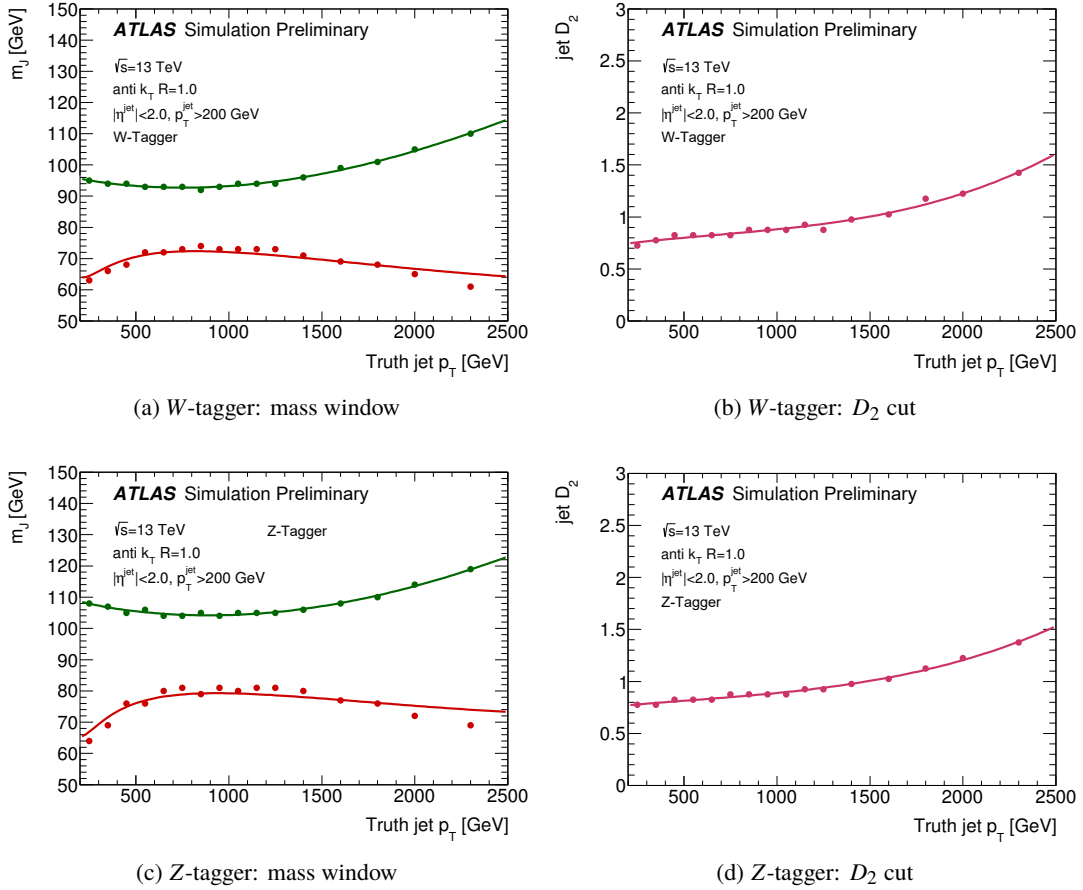(c) Z-tagger: mass window

(d) Z-tagger: $D_2$ cut

Figure 10: Jet mass window (a) and $D_2$ cut (b) of the W-tagger as a function of jet $p_T$. Corresponding values for the Z-tagger are shown in (c) and (d). The initial cut values for maximum significance are shown as solid markers and the fitted parametrizations as solid lines. The tagger is only valid for jets with a $p_T$ between 200 GeV and 2500 GeV and with $|\eta^{\text{jet}}| < 2.0$.
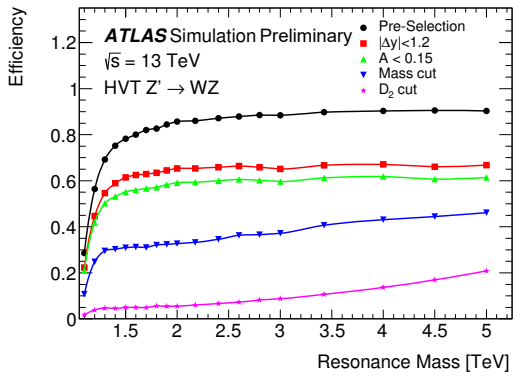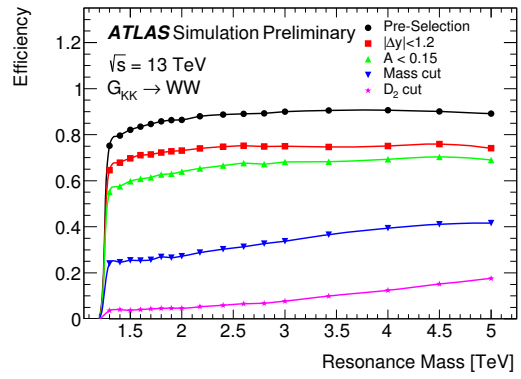
(a) HVT $W' \to WZ$        (b) RS $G_{KK} \to WW$

Figure 11: The efficiency for the selection, defined as the number of selected events at different stages of the selection divided by the number of generated events, of a HVT $W' \to WZ$ and $G_{KK} \to WW$ as a function of mass passing the event selections in sequential. Selections include pre-selections, topological cuts on $|\Delta y_{12}|$, $p_T$ asymmetry, and boson-tagging using jet mass and $D_2$.
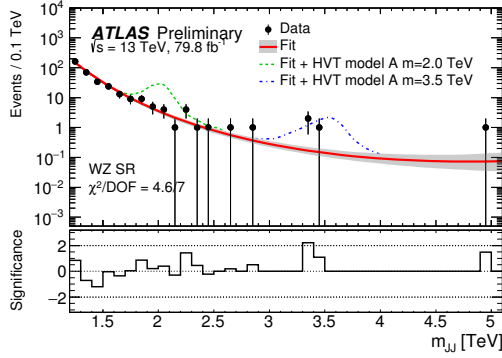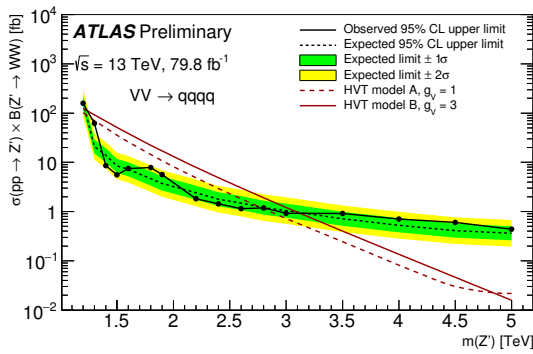
(a) *WZ* selection
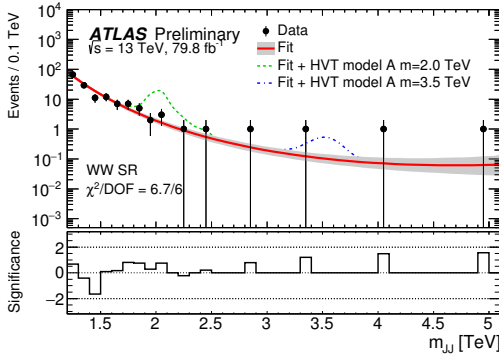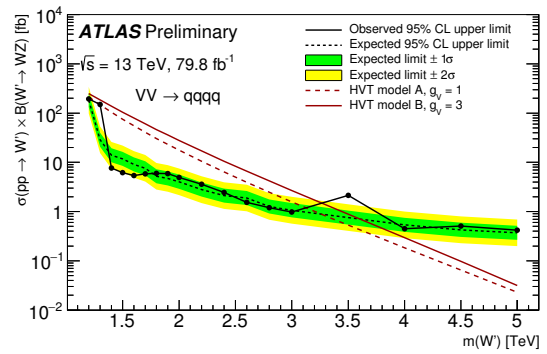


(b) *WW* selection
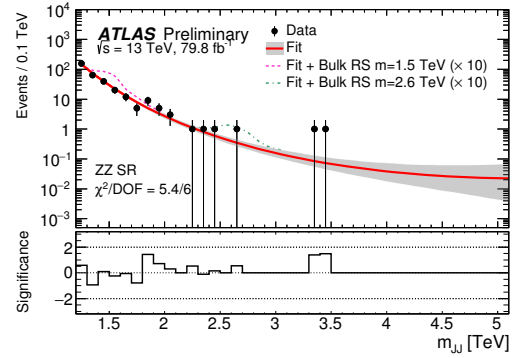


(c) *ZZ* selection

Figure 12: Background-only fits to the dijet mass ($m_{JJ}$) distributions in data in the (a) *WZ*, (b) *WW*, and (c) *ZZ* signal regions. The significance shown in the inset for each bin is the difference between the data and the fit in units of the uncertainty on this difference.



(a) Limits for the HVT $Z' \to WW$



(b) Limits for the $W' \to WZ$

Figure 13: Observed and expected limits at 95% C.L. on cross section times branching ratio as function of (a) $m_{Z'}$ in the *WW* signal selection and (b) $m_{W'}$ in the *WZ* signal region. As the signal regions are not orthogonal, results are not independent in these signal regions.

(a) Limits for Bulk RS graviton decaying to *WW*

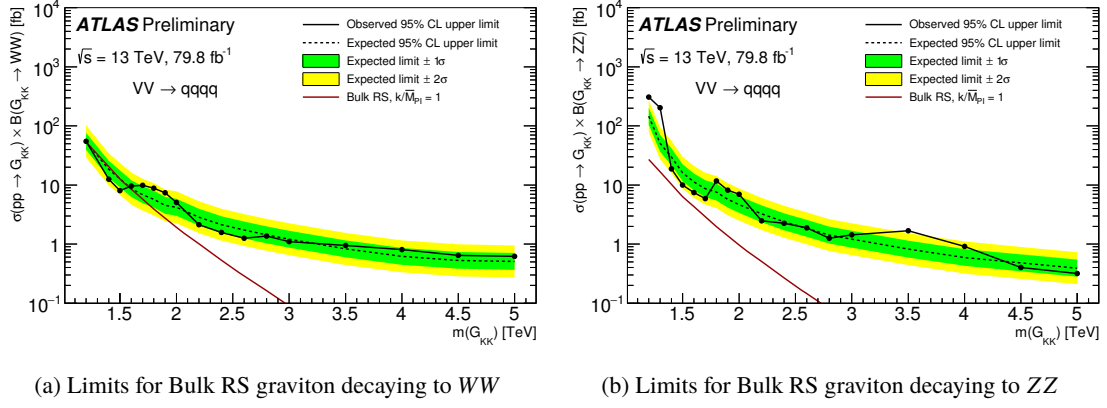(b) Limits for Bulk RS graviton decaying to *ZZ*

Figure 14: Observed and expected limits at 95% C.L. on cross section times branching ratio as function of the Bulk RS graviton $m_{G_{KK}}$ ($k/\overline{M}_{Pl} = 1$) in the (a) *WW*, (b) *ZZ* signal region. As the signal regions are not orthogonal, results are not independent in these signal regions.
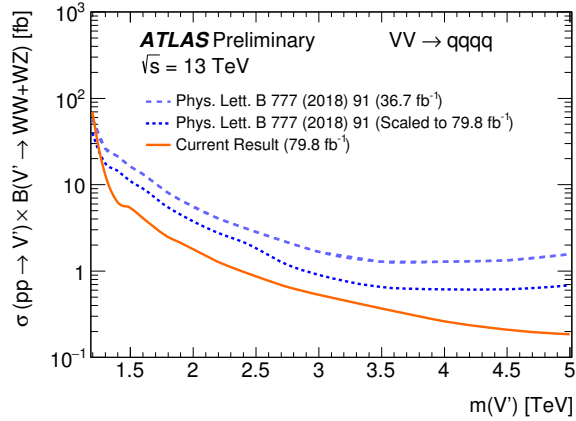


Figure 15: Comparison between the current and previous (Ref. [20]) expected limits at 95% C.L. on cross section times branching ratio for $WW + WZ$ production as a function of $m_{V'}$. An extrapolation of the expected limits from the previous results to the current dataset size, assuming no change to the previous analysis strategy or its uncertainties, is also shown.
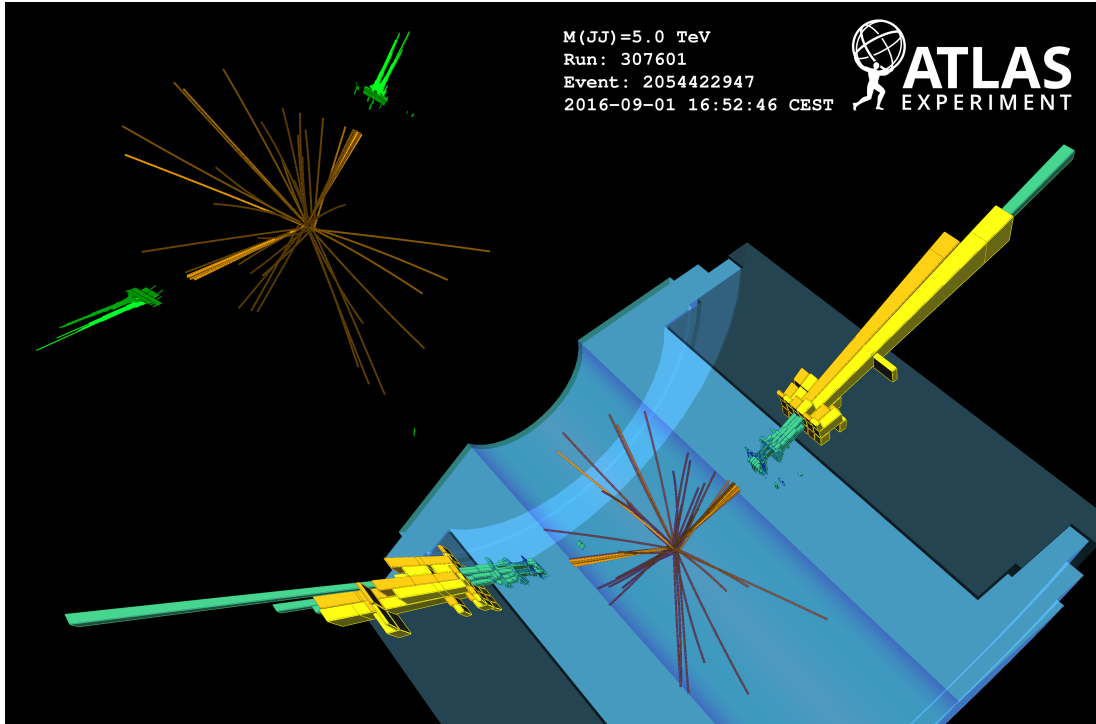
Figure 16: Highest $m_{JJ}$ (= 4993 GeV) diboson candidate event observed in the analysis. Only tracks with $p_T >$ 1.7 GeV are shown in orange, where higher $p_T$ tracks have lighter shades. In the bottom right display, green (yellow and orange) rectangles corresponds to energy deposits in calorimeter cells in different layers of the liquid-argon (hadronic) calorimeter. The top left inset only shows cells of layer 1 of the liquid-argon calorimeter, which has much finer granularity in $\eta$ than any of the other calorimeter layers, but also worse energy resolution. The leading (subleading) jet has a $p_T$ of 2382 GeV (2364 GeV), a mass of 97.8 GeV (65.3 GeV), $\eta = -0.673$ (-0.034) and a $D_2$ of 0.95 (1.43). The average $\mu$ was 23.